Supplementary Information for Manuscript 'Understanding the design of warning signals: a predator's view'

Authors: O. Pennacchio, C.G. Halpin, I.C. Cuthill, P.G. Lovell, M. Wheelwright, J. Skelhorn, C. Rowe, J.M. Harris

Supplementary Information

Description of Table S1: list of species

Table S1 lists all the species in the database and the corresponding information. Each row corresponds to a single species. The rows are ordered by category ('aposematic' or 'non-aposematic'), with aposematic species first and non-aposematic species next, and alphabetically within each category. Columns describe:

Column A, **Species number**: reference number of the species (between 1 and 125);
Column B, **Species**: scientific name of the species;
Column C, **Family**: family of the species;
Column D, **Aposematic, non-aposematic**: 'Aposematic' for aposematic species, 'Non-aposematic' for non-aposematic species;
Column E, **Evidence of palatability, representative paper**: reference for palatability/non-palatability.
Link to Table S1.

Description of Table S2: list of specimens

Table S2 lists all the scans in the database and the corresponding information. Each row corresponds to a single scan. Columns describe:

Column A, **Scan number**: reference number of the scan (between 1 and 662);
Column B, **Species number**: reference number of the species of the specimen (between 1 and 125);
Column C, **Scan name**: filename of the scan (extension format is '*.bil');
Column D, **Species**: scientific name of the species of the scanned specimen;
Column E, **Genus**: genus of the scanned specimen;
Column F, **Family**: family of the scanned specimen;
Column G, **Date scanned**: date of scan acquisition;
Column H, **Aposematic, non-aposematic**: 'Aposematic' for aposematic species, 'Non-aposematic' for non-aposematic species;
Column I, **Collection**: provenance of specimen (museum);
Column J, **Included in analysis***: 'yes' for specimen included in the study, 'no' for specimen not included in the study;
Column K, **Reason for exclusion**: justification for excluding specimens;
Column L, **Luminance energy**: values for the luminance energy summary statistic;
Column M, **Isotropy departure**: values for the isotropy departure summary statistic;
Column N, **Colour energy**: values for the colour energy summary statistic.

*Two scans were discarded from the analysis, Pontia occidentalis_2D_070917 and Thera obeliscata_2D_160517, on the basis that the scans of the ventral sides of the corresponding specimen (Pontia occidentalis_2V_070917 and Thera obeliscata_2V_160517) were not available as we encountered a memory error of the imaging system when scanning them.
Link to Table S2.

Supplementary Methods

Supplementary Method 1

Spatial calibration of hyperspectral imaging system

Hyperspectral imaging systems generally acquire images by translating at constant speed on an object and scanning a single line of pixels ('slit') at a time. To reconstruct a 2-dimensional image in which distance along the slit and distance along the scanning direction are commensurate, the speed of translation of the camera should be set carefully. If the scanning speed is too slow, or respectively too fast, a circle in the image plane will result in an ellipse elongated, respectively contracted, along the direction of scanning in the scanned image. To determine the correct speed of scanning, we used the property that a planar transformation that preserves angles also preserves relative distances. We scanned a calibration paper sheet picturing wedges made of two perpendicular lines and several non-cardinal orientations. All the wedges included the scanning direction in their angular sector. The angles of the wedges in the resulting scanned image were then extracted and compared to 90º using genuine Matlab code ([1]) and the scanning speed was adjusted accordingly. The process was iterated until the average of the measured angles on the scanned image fell within $90º \pm 0.9$.

Supplementary Method 2

Full description of luminance processing model

Edge information. To model the processing of edge information in a pattern, we presented a luminance image to a grid of units that emulate orientation sensitive neurons. We simulated processing of the image by this network of neurons, namely we convolved the luminance images with the receptive fields of the units described below. Convolution is a way to estimate the response of a visual neuron to a location in an image by confronting the feature of its receptive field (here, an oriented edge) with the feature of the image at this location[2]. If the features match, the convolution yields a big number (the neuron becomes active). If the features do not match, the convolution gives a small number (the neuron remains quiescent).

Receptive fields. The model was based on a set of units whose receptive fields are sensitive to edges at different retinotopic locations, different spatial frequencies and orientations, as found in the avian visual system [3-5]. The receptive fields (RFs) of the units were modelled using orientation and spatial frequency sensitive filters using two-dimensional Gabor functions

$$F(x,y) = \exp\left(-\frac{(x\cos\theta+y\sin\theta)^2+\gamma^2(-x\sin\theta+y\cos\theta)^2}{2\,\sigma^2}\right)\cos\left(2\pi f(x\cos\theta + y\sin\theta)+\varphi\right),$$

where x and y respectively give the horizontal and vertical position with respect to the centre of the receptive field, θ is the orientation of the filter, γ is its aspect ratio, φ its phase, σ determines the effective width of the Gaussian envelope of the filter, and f provides the frequency tuning –or spatial scale- of the receptive field. These filters and the chosen parameters have been described in detail elsewhere [6,7]. In the reference model we considered filters tuned to N_θ= 8 evenly distributed orientations ranging between θ = 0º and 157.5º, in steps of 22.5º. The aspect ratio was set to $\gamma = 0.3$ [6,7]. We approximated the modelling of different phases by centring the filters at all pixel locations in the images analysed and set to $\varphi = 0º$. The effective width of the Gabor filters considered depended on the RFs size, Siz, according to the following formula $\sigma = a\,Siz^2 + b\,Siz + c$, with $a = 0.0036$, $b = 0.35$ and $c = 0.18$, and Siz = 25x25, 29x29, 33x33 and 37x37 pixel^2 [6,7], giving values between 11.2 and 18.1. The N_f= 8 different frequencies of the filters were inversely related to the effective width, according to $f = 0.8/\sigma$, giving values ranging from 0.044 to 0.072.

Output of the part of the model based on luminance. The output of the first stage of the model gave a population response, $s(pos, \theta, f)$, where $pos = (x, y)$ represents the topographic locations of the image where a filter (receptive field) is centred, θ is the preferred orientation of the filter and f its preferred spatial frequency. We removed information on the contrast between pattern and background from the population

response of the model by discarding the responses of the filters whose receptive field was not fully included in the area delimited by the pattern. For simplicity, let us still denote $s(pos, \theta, f)$ the population response after this last step.

Normalization and model output. The second component of the model is a divisive normalization. Divisive normalization is a standard normalization process found extensively across sensory systems, in which the activity of a neuron is modulated by the summed activities of a set of neighbouring neurons [8]. Concretely, the responses of the basic units in the model, $s(pos, \theta, f)$, were normalized by the local average activity pooled over spatial locations and orientations [8,9] as

$$r(pos, \theta, f) = \frac{s(pos, \theta, f)}{0.5 + \sum_{\theta', f'} s(pos, \theta', f')/(N_\theta N_f)}.$$

The resulting activity $r(pos, \theta, f)$ was the output of the part of the model based on luminance information, from which the luminance neural signatures were derived.

Full description of colour processing model

To form the response of the model based on colour information, cones' responses were first normalized by their response to a uniform achromatic (i.e., spectrally flat) grey, giving an array of normalized quantum catches q_i for each specimen, with the same spatial resolution as the original for each scan, and for each receptor type $i = U, S, M$ and L. The three chromatic opponent channels were then modelled as[10]

$$L - M = (q_L - q_M)/(q_L + q_M),$$

$$S - U = (q_S - q_U)/(q_S + q_U),$$

$$(L + M) - S = (0.5(q_L + q_M) - q_S)/(0.5(q_L + q_M) + q_S).$$

The output of the part of the model based on colour information was therefore provided by the population activity of the opponent channels, namely $(L - M)(pos)$, $(S - U)(pos)$ and $((L + M) - S)$, where $pos = (x, y)$ represents the topographic locations on the patterns.

Supplementary Method 3

Pattern neural signatures

Luminance energy

The luminance energy for encoding a pattern was computed as the contrast energy of the model encoding activity in response to the pattern, i.e., as the standard deviation of the of the vector of responses $r(pos, \theta, f)$ to the pattern for all locations, all orientations, and all the units in scales 5 to 8 in the model [9,11].

Isotropy departure

To measure pattern isotropy departure, we first considered the evenness of the distribution of the model response to the pattern across orientations at each position pos for each scale f. The responses $r(pos, \theta_i, f)$ to the orientations θ_i were normalized by their sum as $p_i = r(pos, \theta_i, f)/\sum_j r(pos, \theta_j, f)$ to provide a discrete probability distribution, and the evenness of the distribution of the model response was then computed as the Shannon entropy [12] of the corresponding discrete probability distribution as $H(pos, f) = -\sum_{i \epsilon [1, N_\theta]} p_i \log p_i$. In a second step, we computed the mean value for this measure over all locations and spatial scales 5 to 8 for a set of 4096 randomly chosen images in the van Hateren dataset of natural images [13], which yielded our reference isotropy value for natural images, H_{nat} = 2.55 (mathematically possible values range between 0 and $log_2(8) = 3$). Finally, the isotropy departure of a pattern at scale f was computed as the square root of the second moment about the reference value H_{nat} of the vector formed by the local isotropies of a pattern as

$$H_f = \frac{1}{\sqrt{\sum_{pos,f} 1}} \sqrt{\sum_{pos,f} \ (H(pos,f) - H_{nat})^2},$$

where pos ranged over all the locations in the pattern for which the receptive fields of the units was fully included in the area delimited by the pattern (by definition of the $r(pos, \theta_i, f)$, see *Output of the part of the model based on luminance* above). The isotropy departure neural signature was defined as the average value of H_f over scales 5 to 8 of the model. It is worth noting that as isotropy departure is defined as a deviation with respect to a reference value (H_{nat}), even natural scenes have a positive isotropy departure.

Colour energy

The colour energy for encoding a pattern was computed as the contrast energy of the $L - M$ opponent channel, i.e., as the standard deviation of the vector $(L - M)(pos)$ of responses to the pattern of the modelled 'red-green' units [14]. Alternative summary statistics for colour are discussed later.

Supplementary Results

Supplementary Result 1

The neural signature: alternative metrics to quantify pattern and colour

Luminance

Metrics. We considered several alternative summary statistics for the strength of the population response to the Lepidopteran patterns of the part of the model processing luminance. We used:

(a) the average value of the population response, $\frac{1}{N}\sum_{pos,\theta_i,f} r(pos, \theta_i, f)$, where N is the number of units included in the population response, $N = \sum_{pos,\theta_i,f} 1$, and depends on the pattern (see Supplementary Note 2). We call this metric scale-invariant L1-norm (see paragraph 'Scale invariance' below);
(b) the square root of the sum of the squared values of all the units' responses divided by the number of units involved in the population response, $\frac{1}{N}\sqrt{\sum_{pos,\theta_i,f}(r(pos, \theta_i, f))^2}$. We call this metric scale-invariant L2-norm (see paragraph 'Scale invariance' below);
(c) the average response of the 2.5% of the units with the highest response. To compute this value, for each pattern we considered the subpopulation of units with an activity higher than the 97.5% percentile of the distribution of population response and then averaged the response of this subpopulation;
(d) the average response of the 10% of the units with the highest response. To compute this value, for each pattern we considered the subpopulation of units with an activity higher than the 90% percentile of the distribution of population response and then averaged the response of this subpopulation;
(e) The sparsity of the population response to the pattern measured as the kurtosis[15] of the distribution formed by all the units' responses, $r(pos, \theta, f)$.

We also considered a measure directly derived from the luminance of each pattern and not from the model population response to the pattern:

(f), the root mean square (rms) contrast of the luminance image associated with each pattern, defined as $\sqrt{\frac{1}{N}\sum_i (lum(i) - \overline{lum})^2}$, where i runs over all the pixels within the pattern, $lum(i)$ is the luminance of pixel i, $\overline{lum}$ is the average luminance of the pattern, and N is the total number of pixels within the pattern.

Scale invariance. All the metrics except **(e)** are scale-invariant, that is to say they give the same value if a twin population with an identical distribution is added to an initial population. They are therefore all suited to

compare population responses which differ in the number of units involved (because specimens have different sizes), as it is the case for the population responses to the patterns in the database. **(e)** was included because it is a reference measure of the activity of a population of neurons in the literature (see paragraph 'Strength of activity' below).

Strength of activity. All the alternative metrics can be considered measures of pattern strength. Since metrics **(a)** and **(b)** are given by the L1-norm, $\sum_{pos,\theta_i,f} r(pos,\theta_i,f)$, and L2-norm, $\sqrt{\sum_{pos,\theta_i,f}(r(pos,\theta_i,f))^2}$, of the model population response divided by the number N of units involved, they are scale-invariant versions of the L1 and L2-norm of the population response and therefore measure the strength of the model response to a pattern. **(c)** and **(d)** gauge whether part of the model population is particularly strongly activated by a pattern. **(e)** determines whether a pattern in encoded with a sparse code, i.e., a population activity in which only a limited number of units have a strong response and most of the units have a weak response[15]. The higher a value for the kurtosis, the sparser the population response. We chose this metric because delivering a sparse code for natural stimuli has been shown theoretically and empirically to be a plausible goal for early sensory systems. In particular, visual stimuli encountered in natural scenes can be expected to be encoded with a sparser activity than stimuli whose visual features differ from that typically found in nature[15-17].Whereas kurtosis **(e)** is often employed to measure the sparsity of a population response[15,18], it is not scale-invariant and should therefore be considered cautiously when comparing the sparsity of the activity of populations which differ in the number of units involved. Finally, the rms contrast, **(f)**, is a standard measure of contrast in an image, here applied to luminance patterns.

The values for the luminance supplementary statistics for all the scans in the database are available in Table S3 (Link to Table S3). In this table, each row corresponds to a single scan.

Results. We found that all the alternative metrics tell apart AP and non-AP patterns, with AP (n = 96) patterns being associated with a stronger signal than non-AP (n = 29) patterns (Fig. S1). AP patterns had a significantly higher scale-invariant L1 (Fig. S1a, $\chi^2 = 34.1$, df = 1, $p = 5.24 \times 10^{-9}$, ΔAIC = 105.3 – 137.4 = -32.1) and L2-norm (Fig. S1b, $\chi^2 = 14.52$, df = 1, p = 0.00014, ΔAIC = 124.9 – 137.4 = -12.5), a significantly higher average for the activity of the 2.5% (Fig. S1c, $\chi^2 = 48.87$, df = 1, $p = 2.73 \times 10^{-12}$, ΔAIC = 90.5 – 137.4 = -46.9) and 10% (Fig. S1d, $\chi^2 = 46.91$, df = 1, $p = 7.42 \times 10^{-12}$, ΔAIC = 92.5 – 137.4 = -44.9) of the units with a stronger activity, and a significantly higher rms contrast (Fig. S1f, $\chi^2 = 8.50$, df = 1, p = 0.0036, ΔAIC = 130.9 – 137.4 = -6.5). There was a significant difference between the kurtosis of the population response to AP and non-AP patterns with non-AP patterns being associated with a sparser activity than non-AP patterns (Fig. S1e, $\chi^2 = 28.0$, df = 1, $p = 1.21 \times 10^{-7}$, ΔAIC = 111.4 – 137.4 = -26), as would be expected from the bigger similarity between non-AP patterns and natural images.

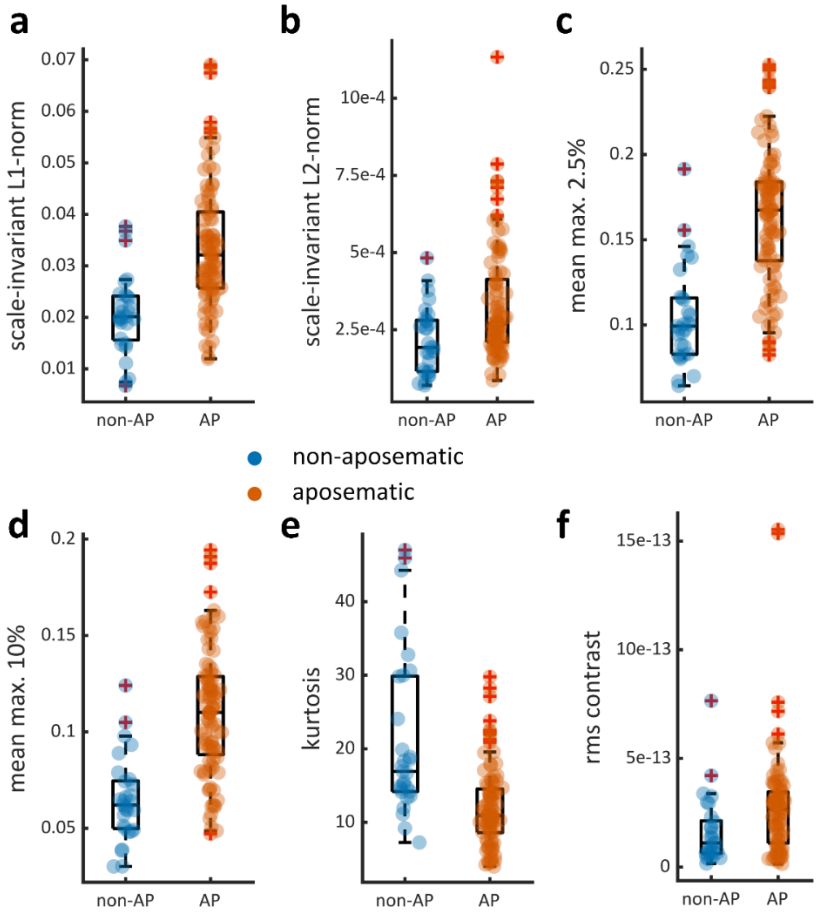

Figure S1. Alternative metrics to quantify patterns based on luminance information. **a**, scale-invariant L1-norm, **b**, scale-invariant L2-norm, **c**, average of activity of the 2.5% of units with highest activity, **d**, average of activity of the 10% of units with highest activity, **e**, kurtosis of the model population activity, and **f**, root mean square contrast of the luminance patterns for all the species in the database, with AP (orange, n = 96) and non-AP (blue, n = 29). All conventions are the same as in Fig. 2 in the main manuscript.

Colour

Metrics. We also considered alternative summary statistics for the strength of the population response of the colour part of the model. We used:

(a) the contrast energy of the $(L+M)-S$ opponent channel, i.e., the standard deviation of the vector $\big((L+M)-S\big)(pos)$ of responses to the pattern of the modelled 'blue-yellow' units;
(b) the contrast energy of the $S-U$ opponent channel, i.e., the standard deviation of the vector $(S-U)(pos)$ of responses to the pattern of the modelled 'blue-ultra-violet' units;
(c) the statistical dispersion of the population response of the 'red-green' channel, $(L-M)(pos)$, measured using the Gini index;
(d) the statistical dispersion of the population response of the 'blue-yellow' channel, $\big((L+M)-S\big)(pos)$, measured using the Gini index;
(e) the statistical dispersion of the population response of the 'blue-ultraviolet' channel, $(S-U)(pos)$, measured using the Gini index.

Scale invariance. All the alternative summary statistics based on colour information are scale-invariant since both the standard deviation and the Gini index are scale invariant.

Strength of activity. The contrast energy of the $(L + M) - S$ and the $S - U$ opponent channels are measures of the strength of activity of the corresponding channels as the main colour summary statistics 'colour energy' is a measure of the strength of activity in the $L - M$ channel. The Gini index measures the extent to what the colour opponent channels are especially stimulated at some location within a pattern.

As for the luminance supplementary statistics, the values for the colour supplementary statistics for all the scans in the database are available in Table S3.

Results. We found that the contrast energy of the 'blue-yellow' ($(L + M) - S$) opponent channel was significantly higher for the AP patterns (n = 96) than for the non-AP patterns (n = 29) patterns (Fig. S2a, χ^2 = 21.47, df = 1, p = 3.60 x 10^{-6}, ΔAIC = 118.0 – 137.4 = -19.4). This result was in line with the separation between AP and non-AP patterns provided by the summary statistics 'colour energy', i.e., the contrast energy of the $L - M$ channel, and the high correlation between the $L - M$ and the $(L + M) - S$ channels for the patterns of the database (Spearman-rank r = 0.87, 95% confidence interval [0.85,0.89]). There was no significant difference in contrast energy of the 'blue-ultraviolet' $(S - U)$ opponent channel (Fig. S2b, χ^2 = 2.48, df = 1, p = 0.1155, ΔAIC = 136.9 – 137.4 = -0.5). The population response of the 'red-green' channel ($(L - M)$) (Fig. S2c, χ^2 = 50.96, df = 1, p = 9.44 x 10^{-13}, ΔAIC = 88.5 – 137.4 = -48.9), the 'blue-yellow' channel $\left((L + M) - S\right)$ (Fig. S2d, χ^2 = 33.1, df = 1, p = 8.72 x 10^{-9}, ΔAIC = 106.3 – 137.4 = -31.1) and the 'blue-ultraviolet' channel ($(S - U)$) (Fig. S2e, χ^2 = 16.45, df = 1, p = 5.0 x 10^{-5}, ΔAIC = 122.0 – 137.4 = -15.4) were more dispersed for the AP patterns than for the non-AP patterns, as shown by the higher Gini indexes.

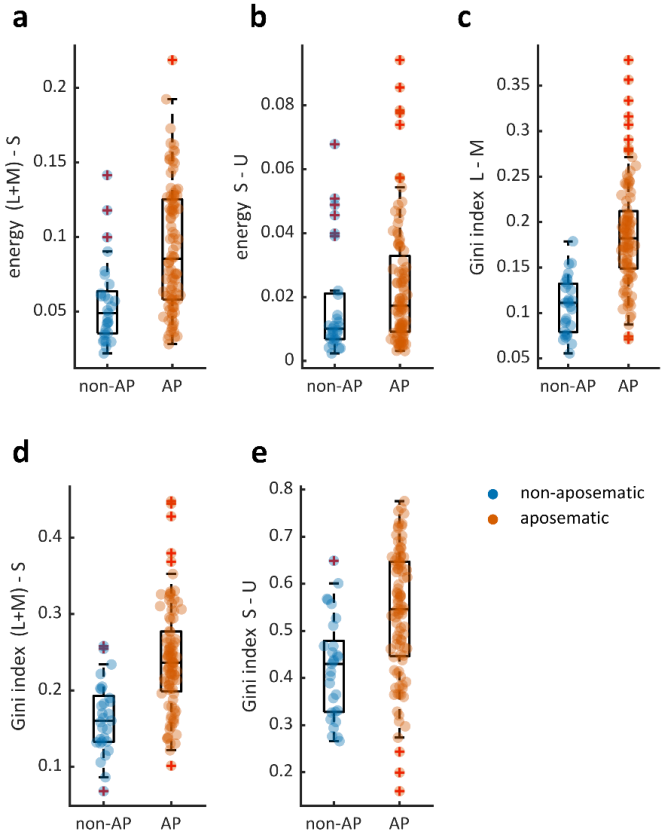

Figure S2. Alternative metrics to quantify patterns based on colour information. a, energy of the population activity of the 'blue-yellow' channel, b, of the 'blue-ultraviolet' channel, c, Gini index of population activity of the 'red-green' channel, d, Gini index of population activity of the 'blue-yellow', e, Gini index of population activity of the 'blue-ultraviolet' in response to AP (orange, n = 96) and non-AP (blue, n = 29) patterns. All conventions are the same as in Fig. 2 in the manuscript.

Supplementary Result 2

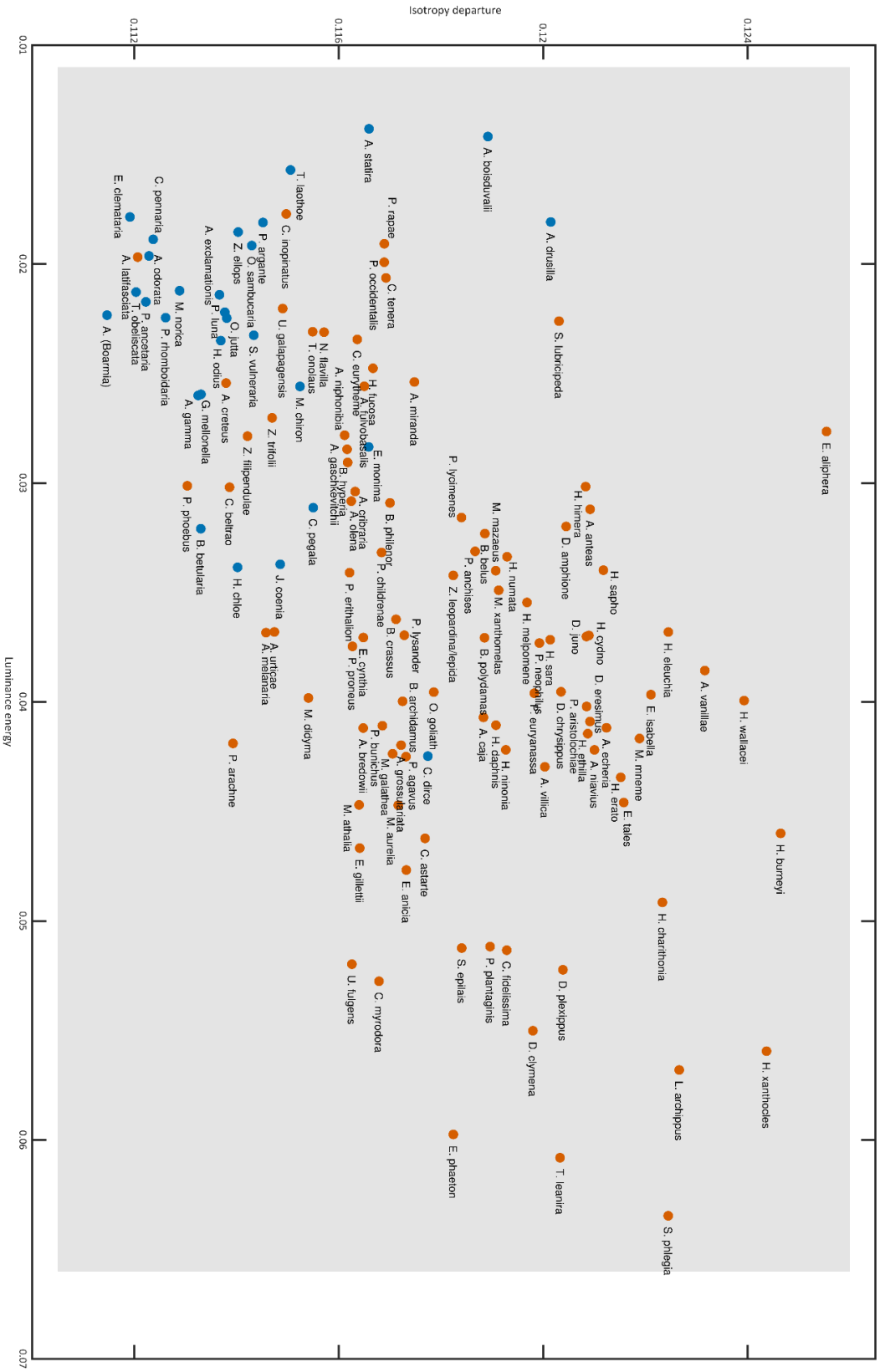

Figure S3. Names of species on luminance pattern space (Fig. 2 manuscript). As in Fig. 2 of the manuscript, each dot represents the average over all specimens and sides (dorsal and ventral) for one of the 125 species in the database (orange, aposematic species; blue, non-aposematic).

Supplementary Result 3

Family-wise comparison of pairs of AP and non-AP patterns

We compared AP and non-AP specimens from the same families to increase the confidence in our overall findings. Five families in our database contained both types of prey (Family, (Number of non-AP species, Number of AP species): Erebidae, (1,12); Geometridae, (9,8); Nymphalidae, (12,49); Pieridae, (4,4); Pyralidae, (1,1)). We followed a bootstrap procedure[19] in which each bootstrap sample consisted of a set of pairs made of an aposematic species and a non-aposematic species within the same family. For each bootstrap sample, we drew the maximum number of pairs in each family, namely N=1 in Erebidae, N=8 in Geometridae, N=12 in Nymphalidae, N=4 in Pieridae and N=1 in Pyralidae, resulting in N=26 pairs. We then computed the category estimate of the main summary statistics (luminance energy, isotropy departure and colour energy) using linear mixed models with 'pattern category' as a fixed factor, 'pair identity' (a number between 1 and 26) as a random factor with random intercept and 'family' as a random effect with both random intercept and random slope. We used N = 1,000,000 bootstrap replicates. Figure S5 shows the luminance energy (Fig. S5a) and isotropy departure (Fig.S5b) summary statistics for all the species in families that contained both aposematic and non-aposematic species as well as an example of random pairing corresponding to the first bootstrap replicate in the series of 1,000,000 replicates.

Luminance energy (all families with both aposematic and non-aposematic species, $p < 10^{-6}$; Erebidae, $p < 10^{-6}$, difference in luminance energy between aposematic and non-aposematic representatives in pairs, 0.0125, 95% confidence interval [0.0036,0.0279]; Geometridae, $p < 10^{-6}$, 0.0087 [0.0074, 0.0100]; Nymphalidae, $p < 10^{-6}$, 0.0143 [0.0110, 0.0177]; Pieridae, $p < 10^{-6}$, 0.0071 [0.0065, 0.0078]) and isotropy departure ($p < 10^{-6}$; Erebidae, $p < 10^{-6}$, difference in isotropy departure between aposematic and non-aposematic representatives in pairs, 0.0051, 95% confidence interval [0.0029,0.0072]; Geometridae, $p < 10^{-6}$, 0.0032 [0.0030, 0.0035]; Nymphalidae, $p < 10^{-6}$, 0.0050 [0.0038, 0.0061]; Pieridae, non-significant, $p = 0.39$, 2.8×10^{-5} [-0.0002, 0.0002]) were significantly higher for AP patterns than for non-AP patterns within the same family. When considering jointly the two luminance neural signatures in the luminance pattern space, we found that within each family the area occupied by AP patterns was shifted towards greater values of energy and isotropy departure with respect to the non-AP patterns (Fig. S6).

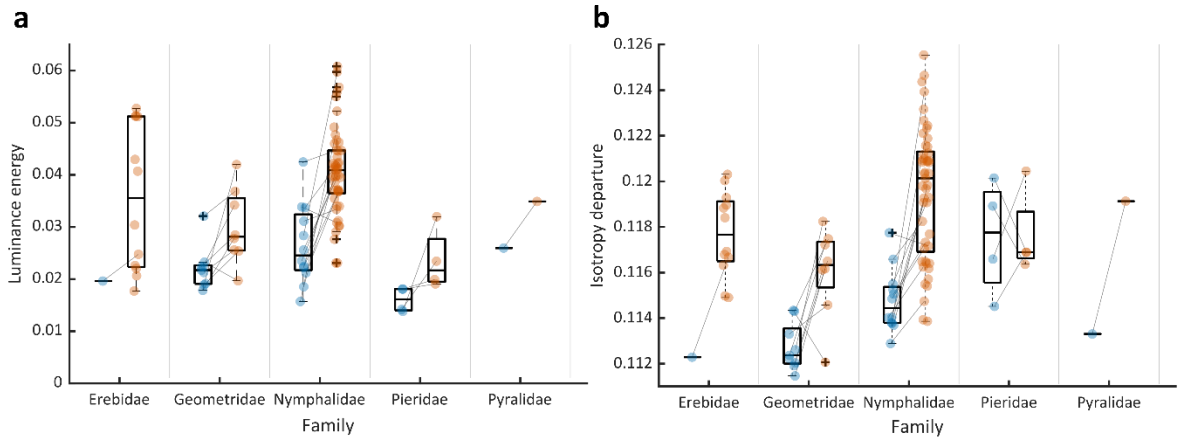

Figure S5. Family-wise comparison of luminance neural signatures within Lepidoptera families. a, b Comparison of the energy (**a**) and isotropy departure (**b**) summary statistics between AP species (orange dots) and non-AP species (blue dots) within the same family for all families in the database that contained both AP and non-AP species (family, total number of species = number of non-AP species + number of AP species: Erebidae, 13 = 1 + 12; Geometridae, 17 = 9 + 8; Nymphalidae, 61 = 12 + 49; Pieridae, 8 = 4 + 4; Pyralidae, 2 = 1 + 1). Values represent the average over all specimen and sides for a given species. All conventions as in Fig. 2 of the manuscript. For the sake of illustration, the grey lines show the pairing given by the first bootstrap.

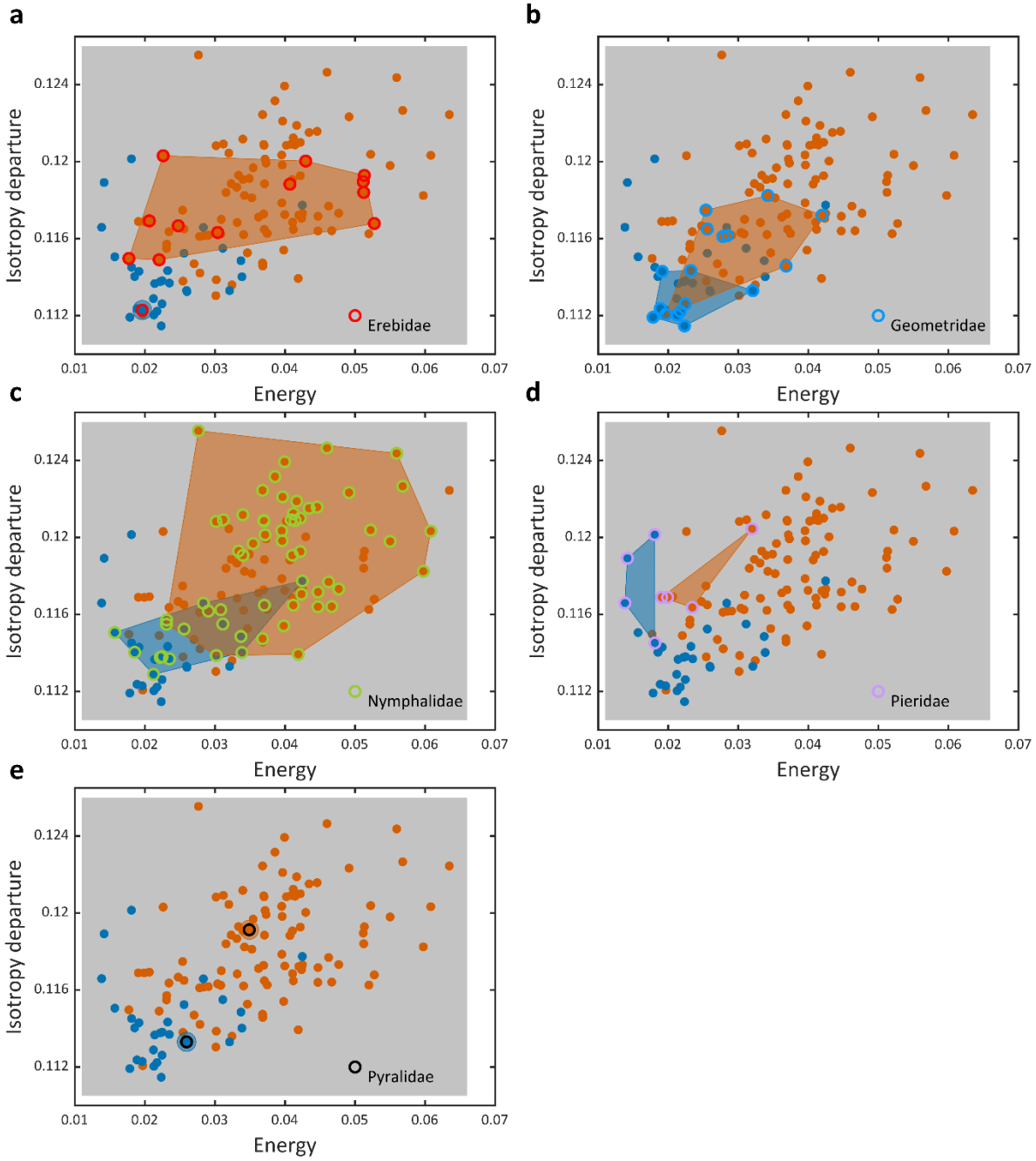

Figure S6. Relative position of AP and non-AP patterns within the same family in the luminance pattern space. **a**,**b**,**c**,**d**,**e**, Scatterplot of the energy and isotropy summary statistics for the model population activity in response to all the Lepidoptera patterns in the database as in Fig. 2, main manuscript, with the species in one of the five families involving both AP and non-AP species (**a**, Erebidae, $N_{non\text{-}AP} = 12$, $N_{AP} = 1$; **b**, Geometridae, $N_{non\text{-}AP} = 8$, $N_{AP} = 9$; **c**, Nymphalidae, $N_{non\text{-}AP} = 49$, $N_{AP} = 12$; **d**, Pieridae, $N_{non\text{-}AP} = 4$, $N_{AP} = 4$; **e**, Pyralidae, $N_{non\text{-}AP} = 1$, $N_{AP} = 1$) singled out. In each panel, the blue, respectively, orange, filled polygon corresponds to the convex hull of the summary statistics (i.e., the smallest convex polygon containing all the points) for all the non-AP, respectively, all the AP species in the family. The plots generally show a displacement towards higher values for energy (i.e., towards the right) and/or isotropy departure (i.e., up) of the areas of the diagnostic landscape spanned by AP species with a given family with respect to the sister or allopatric non-AP species within the same family.

Using the same bootstrap procedure, we found that colour energy was significantly higher for AP than for non-AP patterns (all families with both aposematic and non-aposematic species, $p < 10^{-6}$; Erebidae, $p < 10^{-6}$, difference in colour energy between aposematic and non-aposematic representatives in pairs, 0.0121, 95%

confidence interval [0.0050,0.0308]; Geometridae, $p < 10^{-6}$, 0.0080, [0.0071, 0.0090]; Nymphalidae, $p < 10^{-6}$, 0.0209, [0.0150, 0.0273]; Pieridae, $p < 10^{-6}$, 0.0089, [0.0076, 0.0102]), Fig. S7.

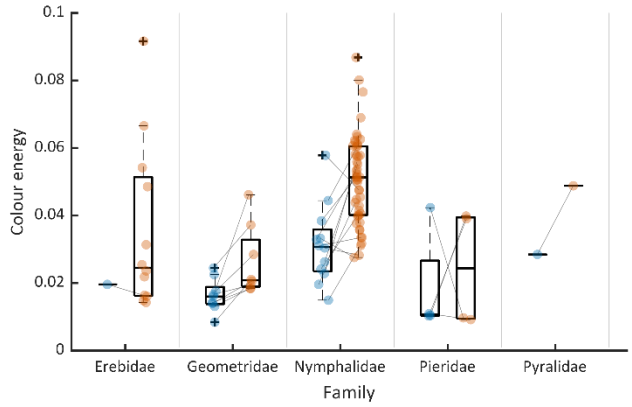

Figure S7. Family-wise comparison of colour neural signature within Lepidoptera families. Comparison of the colour energy summary statistic between AP species and sister or allopatric non-AP species within all families in database that contained both AP and non-AP species. All conventions as in Fig.2 of the manuscript. The grey lines show the pairing given by the first bootstrap..

Supplementary Result 4

Comparison of locations in the luminance energy/isotropy-departure space for AP and non-AP patterns, and natural scenes

We compared locations of AP and non-AP patterns in the 2-dimensional luminance neural signature space (Fig. 2b, main manuscript, and Fig. S8 below). Black points show locations in the space for a database of calibrated natural scenes [13]. Notice that most of the non-AP patterns sit within the 75th percentile of the distribution of values for natural scenes, whilst most of the AP patterns are outside that region.

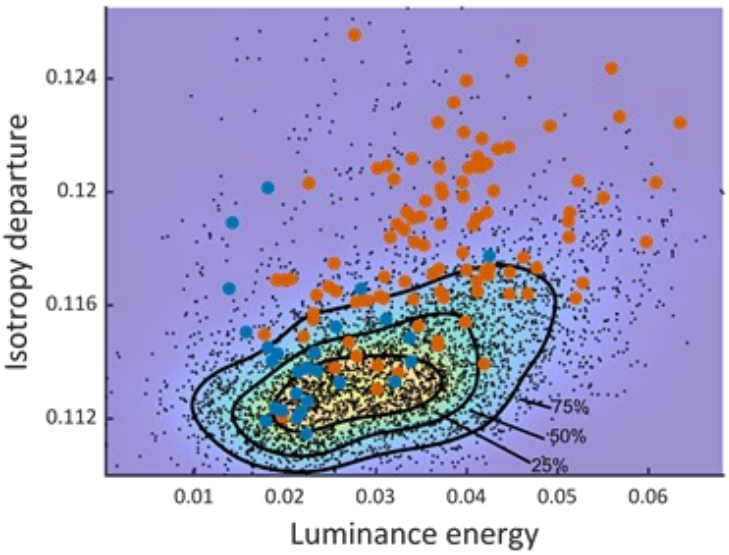

Figure S8. Comparison of luminance neural signatures of aposematic, non-aposematic patterns and natural images. Distribution of energy and isotropy departure for all the species in the database (see Fig. 2 in manuscript) and 4096 patches of natural images from the subset of van Hateren's database of calibrated natural images that do not contain man-made objects. Each black dot corresponds to a single 512 x 512 pixels patch. Black lines show contour for higher 25th, 50th and 75th percentile of the distribution of values for natural patches. Orange points show AP species, blue ones non-AP species.

Supplementary references

1 MATLAB and Statistics Toolbox Release 2015b, The MathWorks, Inc., Natick, Massachusetts, United States.

2 Palmer, S. E. *Vision Science: Photons to Phenomenology*. (MIT Press, Cambridge, Massachusetts, 1999).

3 Engelage, J. & Bischof, H. J. Single cell responses in the ectostriatum of the zebra finch. *J. Comp. Physiol. A -Neuroethol. Sens. Neural Behav. Physiol.* **179**, 785-795 (1996).

4 Pinto, L. & Baron, J. Spatiotemporal frequency and speed tuning in the owl visual wulst. *Eur. J. Neurosci.* **30**, 1251-1268, doi:10.1111/j.1460-9568.2009.06918.x (2009).

5 Li, D. P., Xiao, Q. & Wang, S. R. Feedforward construction of the receptive field and orientation selectivity of visual neurons in the pigeon. *Cereb. Cortex* **17**, 885-893, doi:10.1093/cercor/bhk043 (2007).

6 Serre, T., Oliva, A. & Poggio, T. A feedforward architecture accounts for rapid categorization. *Proc. Natl. Acad. Sci. U. S. A.* **104**, 6424-6429, doi:10.1073/pnas.0700622104 (2007).

7 Serre, T. & Riesenhuber, M. Realistic modeling of simple and complex cell tuning in the HMAX model, and implications for invariant object recognition in cortex. Report No. AI Memo 2004-017, CBCL Memo 239, (MIT, 2004).

8 Carandini, M. & Heeger, D. J. Normalization as a canonical neural computation. *Nature Reviews Neuroscience* **13**, 51-62, doi:10.1038/nrn3136 (2012).

9 Kay, K. N., Winawer, J., Rokem, A., Mezer, A. & Wandell, B. A. A Two-Stage Cascade Model of BOLD Responses in Human Visual Cortex. *PLoS Comput. Biol.* **9**, doi:10.1371/journal.pcbi.1003079 (2013).

10 Osorio, D., Vorobyev, M. & Jones, C. D. Colour vision of domestic chicks. *J. Exp. Biol.* **202**, 2951-2959 (1999).

11 Watson, A. B., Barlow, H. B. & Robson, J. G. What does the eye see best? *Nature* **302**, 419-422, doi:10.1038/302419a0 (1983).

12 Cover, T. M. & Thomas, J. A. *Elements of Information Theory*. (Wiley-Interscience, 2006).

13 van Hateren, J. H. & van der Schaaf, A. Independent component filters of natural images compared with simple cells in primary visual cortex. *Proceedings of the Royal Society B-Biological Sciences* **265**, 359-366 (1998).

14 Chaparro, A., Stromeyer, C. F., Huang, E. P., Kronauer, R. E. & Eskew, R. T. Color is what the eye sees best. *Nature* **361**, 348-350, doi:10.1038/361348a0 (1993).

15 Olshausen, B. A. & Field, D. J. Sparse coding of sensory inputs. *Curr. Opin. Neurobiol.* **14**, 481-487, doi:10.1016/j.conb.2004.07.007 (2004).

16 Olshausen, B. A. & Field, D. J. Emergence of simple-cell receptive field properties by learning a sparse code for natural images. *Nature* **381**, 607-609, doi:10.1038/381607a0 (1996).

17 Vinje, W. E. & Gallant, J. L. Sparse coding and decorrelation in primary visual cortex during natural vision. *Science* **287**, 1273-1276, doi:10.1126/science.287.5456.1273 (2000).

18 Hyvarinen, A., Hurri, J. & Hoyer, P. O. *Natural Image Statistics A Probabilistic Approach to Early Computational Vision Introduction*. Vol. 39 (Springer-Verlag London, 2009).

19 Efron, B. & Tibshirani, R. J. *An introduction to the bootstrap*. (New York: Chapman & Hall, 1993).